

TECHNICAL NOTE

Quantifying stress-induced anisotropy using inter-void constrictions

T. SHIRE*, C. O’SULLIVAN*, D. BARRETO† and G. GAUDRAY‡

In particulate geomechanics it is common to quantify fabric anisotropy using contact and particle orientations. Measurement of void anisotropy is less common, most likely owing to the difficulties associated with defining individual voids. Here a Delaunay tessellation-based approach is applied to measure anisotropy of the inter-void constriction orientations. This new measure of fabric anisotropy was capable of identifying stress-induced anisotropy in discrete-element modelling true triaxial simulations with spherical particles. A relationship is established between the constriction orientations, the macro-scale principal stress directions and the micro-scale contact normal orientations.

KEYWORDS: anisotropy; discrete-element modelling; fabric/structure of soils

INTRODUCTION

Soil anisotropy in a soil is either inherent or induced (e.g. Casagrande & Carillo, 1944). Typically geomechanics observations of anisotropy have focused on the overall material behaviour, that is the strength (e.g. Arthur & Menzies, 1972), stiffness (e.g. Kuwano & Jardine, 2002) and permeability (e.g. Chan & Kenney, 1973). These observations of macro-scale material response are manifestations of a particle-scale fabric anisotropy. Using particle-scale data the fabric can be quantified using the following data sets (Oda *et al.*, 1985; Fonseca, 2011)

- (a) contact normal orientations
- (b) particle orientations
- (c) void orientations
- (d) branch vector orientations.

Earlier studies quantifying fabric and relating it to the overall material response have mostly used data from photo-elastic tests and discrete-element modelling (DEM) simulations (e.g. Oda *et al.*, 1985; Thornton, 2000; Ng, 2001), and have considered mainly the particle or contact orientations. In contrast, studies of void orientation anisotropy have been less common, especially for three-dimensional (3D) granular materials. This is probably a consequence of the difficulty in identifying individual voids within a continuous 3D void space. Fonseca (2011) applied watershed segmentation and principal component analysis to identify void orientations in 3D micro-computed tomography images of sand samples. In two dimensions, Ghedia & O’Sullivan (2012) also used watershed segmentation to extend the scan-line method proposed by Oda *et al.* (1985). Descriptions of techniques to measure anisotropy, including void anisotropy, from two-dimensional (2D) scanning electron microscope (SEM) images of clay samples can be found in Smart (1991) and Tovey *et al.* (1992), among other references.

This technical note presents a new method for measuring void anisotropy using the inter-void constrictions, that is the ‘throats’ between two distinct voids. This void constriction anisotropy is calculated for a DEM dataset in which anisotropy was stress induced. The void constriction and contact normal anisotropies are compared. This new measure of fabric provides additional insight into the particle-scale material response to deviatoric stress.

ALGORITHM

The Delaunay tessellation-based algorithm used here was originally proposed by Reboul (2008) and Reboul *et al.* (2010). In this algorithm a set of tetrahedra formed by a Delaunay tessellation of the particle centroids is used. The inter-void constrictions are identified using the faces of these tetrahedra (Fig. 1). On each face the constriction diameter is taken to be the diameter of the smallest circle that can be inscribed on that face between the three particles that form that face. A further check is applied to ensure that this circle does not overlap with any other particle that intersects the tetrahedron face.

In order to avoid the over-segmentation of void space, adjacent tetrahedra may be merged using a criterion proposed by Al-Raoush *et al.* (2003). The scheme can be understood by reference to a simple two-dimensional (2D)

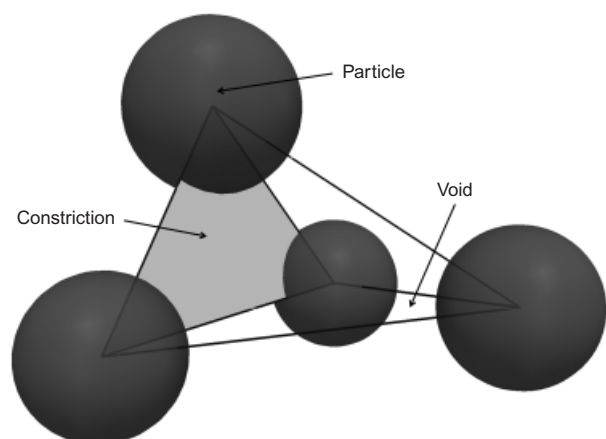


Fig. 1. Description of void characteristics using Delaunay cell

Manuscript received 21 December 2011; revised manuscript accepted 15 June 2012. Published online ahead of print 21 September 2012. Discussion on this paper closes on 1 June 2013, for further details see p. ii.

* Department of Civil and Environmental Engineering, Imperial College London, UK.

† School of Engineering and the Built Environment, Edinburgh Napier University, UK

‡ École des Ponts ParisTech, Paris, France.

scenario of uniform particles on a square grid, as illustrated in Fig. 2. Fig. 2(a) illustrates the constriction locations. The Delaunay triangulation to identify the voids is presented in Fig. 2(b). As illustrated in Fig. 2(c) if circles are fitted to each of these edge gaps the voids are essentially over-segmented; in other words, a space that would intuitively be considered a single void is subdivided. As illustrated in Fig. 2(d), spheres that are tangential to each of the particles forming a Delaunay cell are identified. Then the overlap between this sphere and each of the spheres in adjacent Delaunay cells is calculated and, if this overlap exceeds a user-specified value, the cells are merged to form a single void cell (Al-Raoush *et al.*, 2003; Reboul, 2008). The choice of overlap is subjective; a smaller critical overlap results in the formation of fewer, larger voids. An overlap criterion of $O = 50\%$ is used here, calculated as

$$O = \frac{x_1 - x_2}{\min(r_1, r_2)} \times 100 \quad (1)$$

where x_1 , x_2 and r_1 , r_2 are the centroidal positions and radii of two adjacent inscribed spheres. This method suffers from the same drawback as the watershed segmentation approach used by Fonseca (2011); that is the larger constrictions identified may not be real void boundaries, but narrow points within valid voids. It is important to realise that in a soil sample with interconnected voids the exact definition of boundaries between all voids in the system will always be subjective and over-segmentation of the void space is likely, whatever method is used.

This approach does not generate information on the topology of the real pores, but rather coordinates of the vertices of the particles surrounding a void are given, and these particles are considered to form a 'void cell'. To describe the true void geometry it would be necessary to

consider the segments of the surfaces of the spheres that intersect the void cell faces, which is a non-trivial operation. Here full information on the constrictions is, however, available. To assess the void fabric, the algorithm was therefore extended to measure the constriction orientations by recording the Cartesian unit vectors normal to the constriction face (Gaudray, 2011). The algorithm implementation was successfully validated using regular packings of uniform spheres, for which analytical expressions for constriction size and orientations are known.

DEM SIMULATIONS

In the current study ten virtual DEM samples from simulations detailed by Barreto (2009) and Barreto & O'Sullivan (2012) were analysed, as listed in Table 1. The PSD of the spheres matched physical glass bead samples, and is given in Fig. 3 for percentage smaller both by number and volume. The samples were created by generating a cloud of non-contacting spheres with random locations within a periodic cell. The samples were compressed isotropically and monotonically to a mean normal stress of 200 kPa, following which a series of strain-controlled, constant mean stress, constant intermediate principal stress ratio, true triaxial compression tests were performed. The intermediate stress ratio is defined as

$$b = \frac{\sigma_2 - \sigma_3}{\sigma_1 - \sigma_3} \quad (2)$$

where σ_1 , σ_2 and σ_3 are the major, intermediate and minor principal stresses. The series included tests with $\sigma_1 = \sigma_2$ ($b = 1$) and $\sigma_2 = \sigma_3$ ($b = 0$) and these are referred to as triaxial compression (TXC) and triaxial extension (TXE) respectively. Tests with $b = 0.4$ that had approximately plane

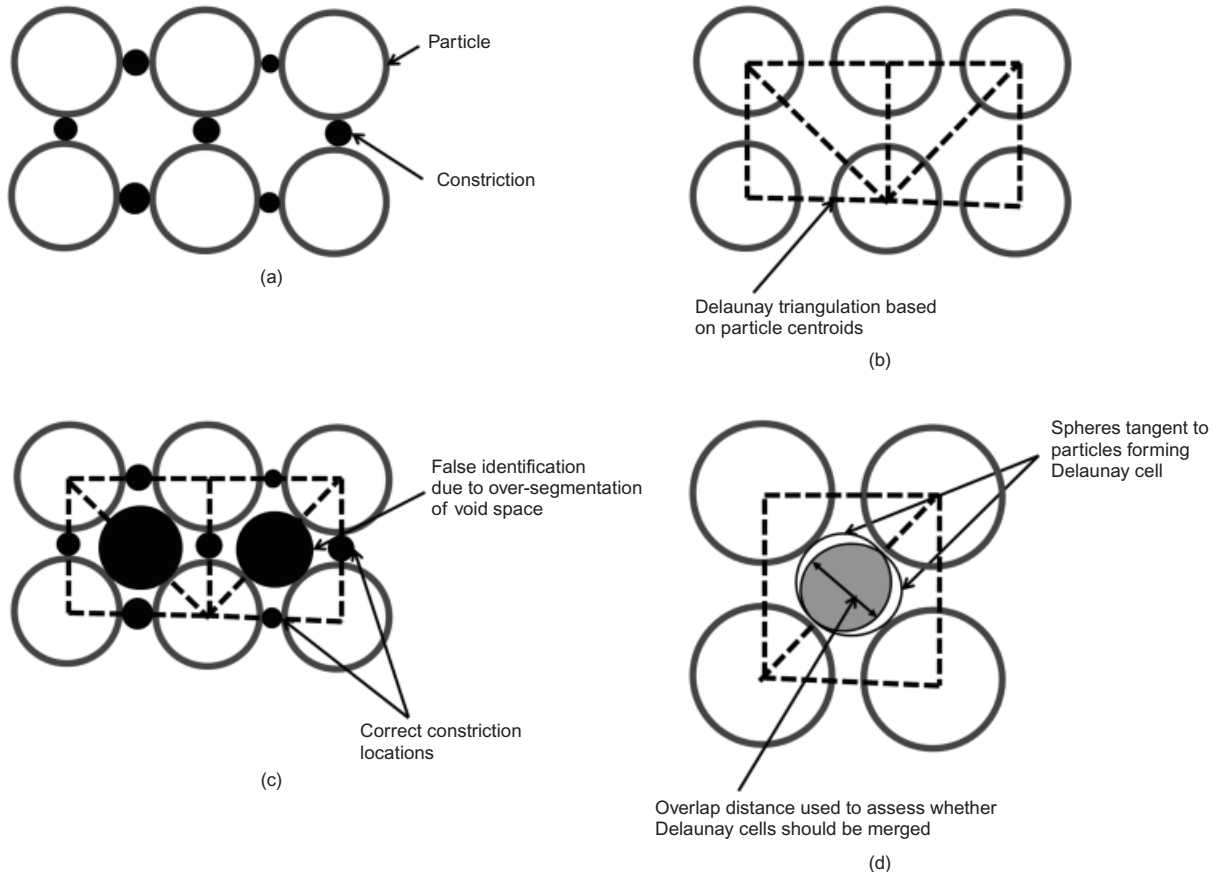
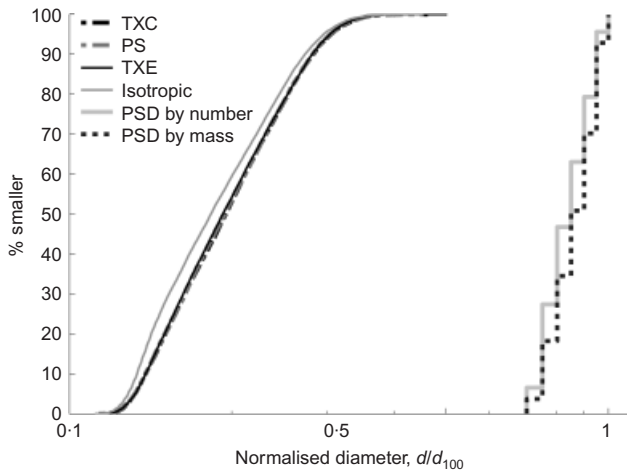


Fig. 2. Merging of Delaunay cells to form voids (adapted from Al-Raoush *et al.* (2003))

Table 1. Macroscopic variables for true-triaxial samples analysed

| Sample | Coefficient of interparticle friction, μ | Void ratio, e , at $\varepsilon_d = 10\%$ | Deviatoric stress, J : kPa at $\varepsilon_d = 10\%$ | ϕ'_{peak} |
|-----------------------|--|---|--|-----------------------|
| Triaxial compression | 0.14 | 0.562 | 87 | 21.92 |
| | 0.325 | 0.572 | 101 | 26.71 |
| | 0.70 | 0.581 | 101 | 28.44 |
| Triaxial extension | 0.14 | 0.559 | 74 | 24.17 |
| | 0.325 | 0.568 | 85 | 29.35 |
| | 0.70 | 0.576 | 85 | 31.01 |
| Plane strain | 0.14 | 0.560 | 81 | 26.25 |
| | 0.325 | 0.570 | 94 | 31.92 |
| | 0.70 | 0.577 | 92 | 33.72 |
| Isotropic compression | All values | 0.529 | 0 | N/A |


 Fig. 3. Particle size distributions by number and volume, CSDs by number for initial isotropic stress state and following shearing to $\varepsilon_d = 10\%$

strain conditions ($\varepsilon_2 < 0.05\%$) are also presented and referred to as PS. Each test series was repeated using three coefficients of inter-particle friction, $\mu = 0.14, 0.325$ and 0.7 . The sample void ratios increased with μ . All samples dilated during shearing from the isotropic state. The results presented in this paper consider the fabric anisotropy at 10% deviatoric strain (ε_d), where

$$\varepsilon_d = \frac{2}{\sqrt{6}} \sqrt{(\varepsilon_1 - \varepsilon_2)^2 + (\varepsilon_2 - \varepsilon_3)^2 + (\varepsilon_3 - \varepsilon_1)^2} \quad (3)$$

and $\varepsilon_1, \varepsilon_2$ and ε_3 are the major, intermediate and minor principal strains.

The void ratio, e , and deviatoric stress, J , values for the samples considered are presented in Table 1, where

$$J = \frac{1}{\sqrt{6}} \sqrt{(\sigma'_1 - \sigma'_2)^2 + (\sigma'_2 - \sigma'_3)^2 + (\sigma'_3 - \sigma'_1)^2} \quad (4)$$

and σ'_1, σ'_2 and σ'_3 are the major, intermediate and minor principal effective stresses. Fig. 4 illustrates the variation in J with ε_d for the simulation with $\mu = 0.325$. The peak angles of shearing resistance ($\phi'_{\text{peak}} = \sin^{-1}[(\sigma'_1 - \sigma'_3)/(\sigma'_1 + \sigma'_3)]$) for each simulation are listed in Table 1. As discussed further by Barreto & O'Sullivan (2012) and Barreto (2009) the observed material response is in line with previous DEM and experimental studies. As the samples are relatively dense with a relatively uniform particle size distribution, there is an initial stiff response. Such a response is typical

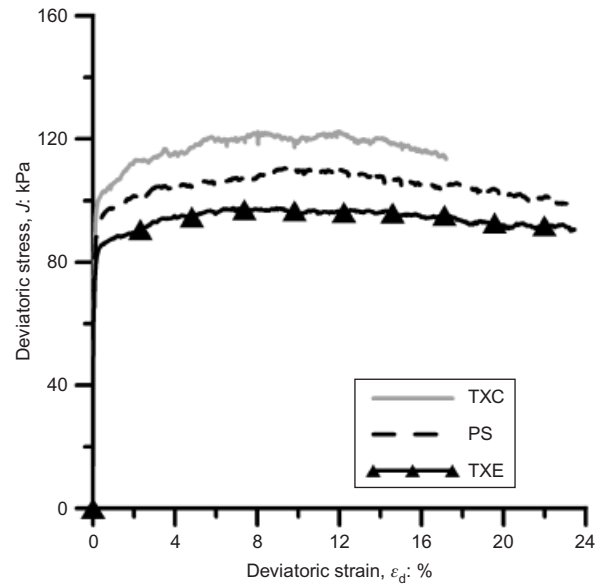


Fig. 4. Deviatoric stress with deviatoric strain level

for this type of sample and is termed a type 1 response by Roux & Combe (2010). A similar initial stiff response was noted by Ng (2004a) in his true triaxial DEM simulations using ellipsoidal particles and by Thornton (2000) using spherical particles. The pattern of variation in ϕ'_{peak} with b is similar to those reported in experimental studies of Sutherland & Mesdary (1969) and Haruyama (1981) and also to the DEM simulations of Ng (2004b). Additionally, the DEM true triaxial studies of Thornton (2000), Ng (2004a) and Barreto & O'Sullivan (2012) have been compared against the Lade & Duncan (1973) failure criterion in terms of failure stress state and have demonstrated a reasonable agreement.

RESULTS

The constriction size distributions (CSDs) by percentage number smaller for $\mu = 0.325$ are included in Fig. 3. In comparison with the initial, isotropic stress state, the constriction diameters generally increased during shearing. This is unsurprising given that all the samples underwent dilation, leading to an increase in void space. The CSDs at $\varepsilon_d = 10\%$ for each shearing mode are similar.

The fabric anisotropy is quantified using the unit vectors normal to the constrictions and the inter-particle contacts and applying the fabric tensor as defined by Satake (1982)

$$\Phi_{ij} = \frac{1}{N} \sum_{k=1}^N \mathbf{n}_i^k \mathbf{n}_j^k \quad (5)$$

where N is the total number of vectors and \mathbf{n}_i^k is the k th unit orientation vector. Just as in the case of the stress tensor, the principal components of the fabric tensor (Φ_1, Φ_2, Φ_3), can be obtained through eigenvalue analysis. The 3D deviatoric fabric, Φ_d , can be calculated using the following invariant as proposed by Barreto *et al.* (2009)

$$\Phi_d = \frac{1}{\sqrt{2}} \sqrt{(\Phi_1 - \Phi_2)^2 + (\Phi_2 - \Phi_3)^2 + (\Phi_3 - \Phi_1)^2} \quad (6)$$

Table 2 gives data on the deviatoric fabric for both inter-particle contacts and inter-void constrictions for each test at $\varepsilon_d = 10\%$. Three values for the constriction Φ_d are given considering

- (a) all constrictions
- (b) constrictions with diameter $d_c < d_{c50}$ (d_{c50} is the median d_c)
- (c) the smallest 15% of constrictions, having $d_c < d_{c15}$.

Quantifying fabric using the smaller constrictions removes the uncertainty associated with the larger constrictions, which may represent local narrowing of voids, rather than

being valid void–void boundaries. The overall constriction distribution shows little fabric anisotropy. However, anisotropy increases markedly as a smaller range of constrictions is considered. The intensity of the constriction anisotropy for the range $d_c < d_{c15}$ is related to the shearing mode in the order $\text{TXE} > \text{PS} > \text{TXC}$. The volumetric strain data indicate that no sample is at a critical state at this strain level.

The directional distribution of contacts and constrictions can be visualised using 2D rose histograms. Here each histogram bin represents an angular interval in a plane normal to a principal stress direction and each bin is shaded according to the average magnitude of its members. In each test the z -direction corresponds to σ_1 , y -direction to σ_2 and x -direction to σ_3 (note that in triaxial compression $\sigma_2 = \sigma_3$ and in extension $\sigma_1 = \sigma_2$). A fabric ellipsoid calculated using the Fourier series (Rothenburg & Bathurst, 1989; Barreto *et al.*, 2008) has been fitted to each set of histogram data for all the constrictions, for constrictions with $d_c < d_{c15}$ and for the contact normals and are presented in Figs 5, 6 and 7 for TXC, PS and TXE respectively.

Figure 5 shows that the contact normals are preferentially oriented in the σ_1 direction (z -direction) and the average contact force is largest in the σ_1 direction. No preferential direction of the overall constriction numbers can be seen in any direction (the fabric ellipsoids in Figs 5(d)–5(f) are all

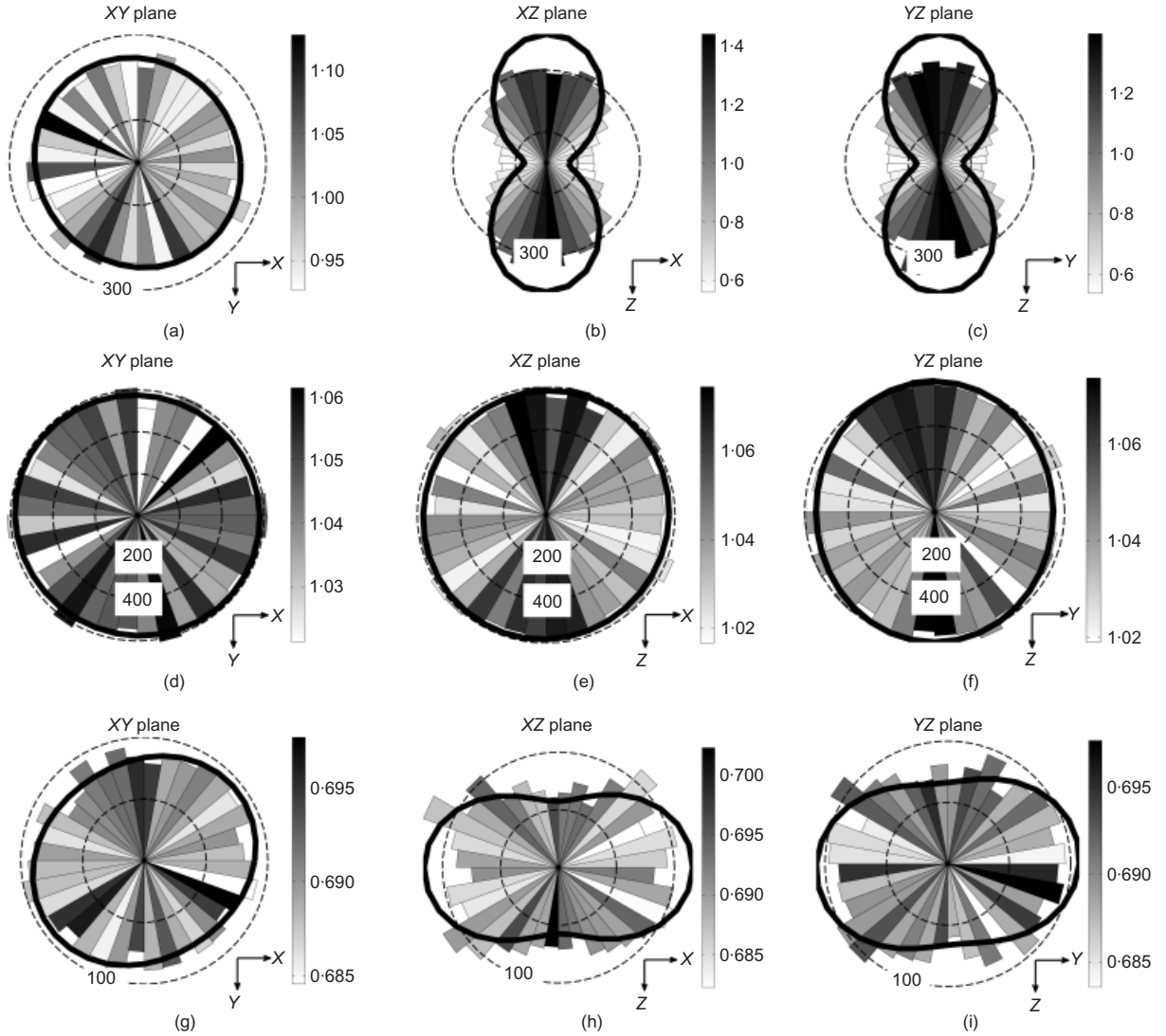
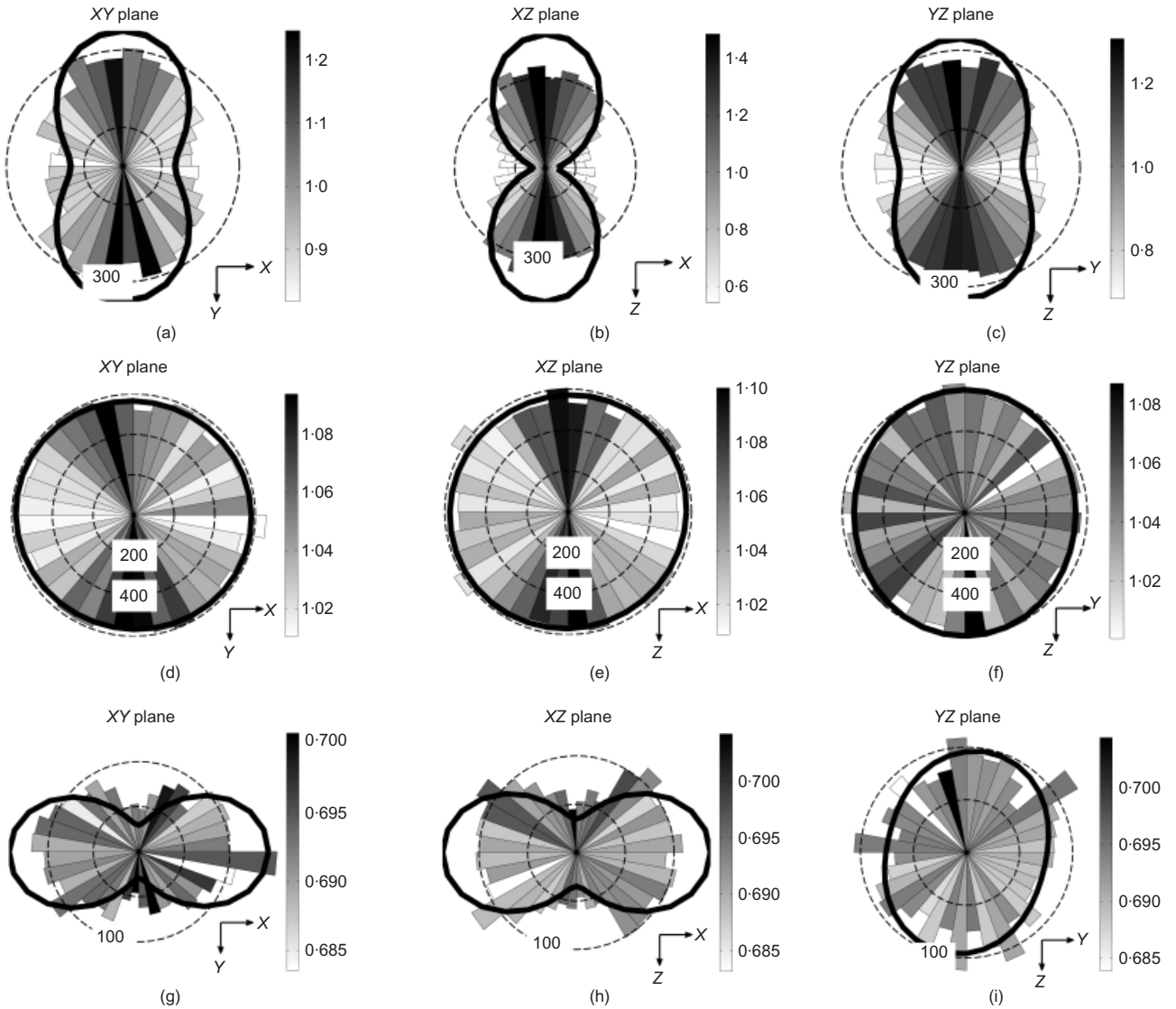


Fig. 5. Rose histograms for triaxial compression sample at $\varepsilon_d = 10\%$: (a)–(c) particle contact normals; (d)–(f) all constriction normals; (g)–(i) constriction normals $d_c < d_{c15}$. Shading indicates average: (a)–(c) normalised contact force $f = N/\langle N \rangle$; (d)–(i) normalised constriction diameter d_c/d_{c50}

Table 2. Deviatoric fabric for true-triaxial samples: $\varepsilon_d = 10\%$

| Sample | Coefficient of interparticle friction, μ | Constriction deviatoric fabric (all constriction normals) | Constriction deviatoric fabric ($d_c < d_{c50}$ constriction normals) | Constriction deviatoric fabric ($d_c < d_{c15}$ constriction normals) | Contact normal deviatoric fabric (all particles) | Deviatoric strain, ε_d : % |
|-----------------------|--|---|--|--|--|--|
| Triaxial compression | 0.14 | 0.003 | 0.025 | 0.069 | 0.111 | 10 |
| | 0.325 | 0.006 | 0.024 | 0.071 | 0.137 | 10 |
| | 0.70 | 0.004 | 0.028 | 0.072 | 0.152 | 10 |
| Plane strain | 0.14 | 0.005 | 0.031 | 0.110 | 0.122 | 10 |
| | 0.325 | 0.005 | 0.033 | 0.116 | 0.144 | 10 |
| | 0.70 | 0.005 | 0.035 | 0.117 | 0.151 | 10 |
| Triaxial extension | 0.14 | 0.005 | 0.034 | 0.131 | 0.120 | 10 |
| | 0.325 | 0.007 | 0.036 | 0.131 | 0.144 | 10 |
| | 0.70 | 0.004 | 0.039 | 0.146 | 0.159 | 10 |
| Isotropic compression | All values | 0.005 | 0.005 | 0.019 | 0.007 | 0 |

**Fig. 6.** Rose histograms for plane strain sample at $\varepsilon_d = 10\%$: (a)–(c) particle contact normals; (d)–(f) all constriction normals; (g)–(i) constriction normals $d_c < d_{c15}$. Shading indicates average: (a)–(c) normalised contact force $f = N / \langle N \rangle$; (d)–(i) normalised constriction diameter d_c / d_{c50}

approximately circular). This agrees with the low deviatoric fabric values in Table 2. However, anisotropy is observed in the average diameter of the constrictions, with larger average constrictions found in the σ_1 direction. Figs 5(g)–5(i) show

that the smallest constrictions are preferentially aligned away from the σ_1 direction. Similar patterns can be observed for plane strain and triaxial extension in Figs 6 and 7 respectively, with preferential orientation of inter-particle contacts

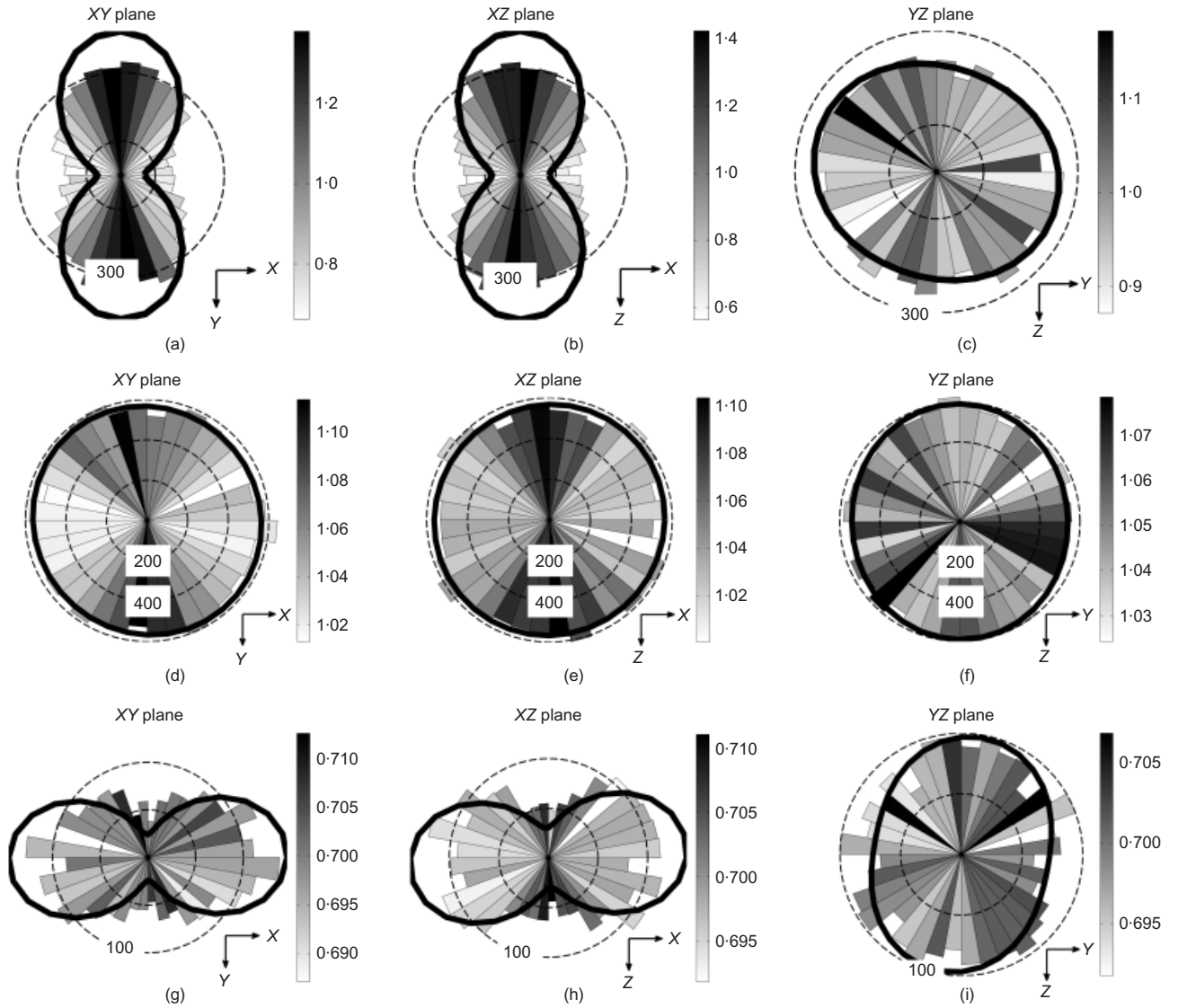


Fig. 7. Rose histograms for triaxial extension sample at $\epsilon_d = 10\%$: (a)–(c) particle contact normals; (d)–(f) all constriction normals; (g)–(i) constriction normals $d_c < d_{c15}$. Shading indicates average: (a)–(c) normalised contact force $f = N/\langle N \rangle$; (d)–(i) normalised constriction diameter d_c/d_{c50}

and larger average constrictions in the direction of the larger principal stress in that plane, and smaller constrictions preferentially orientated orthogonal to this in the direction of the smaller principal stress.

Oda *et al.* (1985) showed that during biaxial compression of photoelastic rods voids become elongated with the void long axis aligned in the σ_1 direction. The data presented here support this observation for a 3D material. Referring to the schematic diagram presented in Fig. 8, the larger constrictions have contact normals orientated in the vertical direction. This indicates that voids are opening up between quasi-parallel strong force chains that transmit the deviatoric stress through the sample. The prevalence of small constrictions with normals orthogonal to the major principal stress direction reflects the presence of void boundaries that are clearly defined at the strong force chains. Note that while force chains are sometimes associated with shear bands (e.g. experimental work of Rechenmacher *et al.* (2010)), force chains, which represent a preferential orientation in the contact normals, can form even at very low strain levels, provided there is an anisotropic stress state. Graphical evidence of this can be found in Rothenburg & Bathurst (1989) and Behringer *et al.* (2008), among many others. As the current simulations were carried out in a periodic cell, the development of shear bands that can

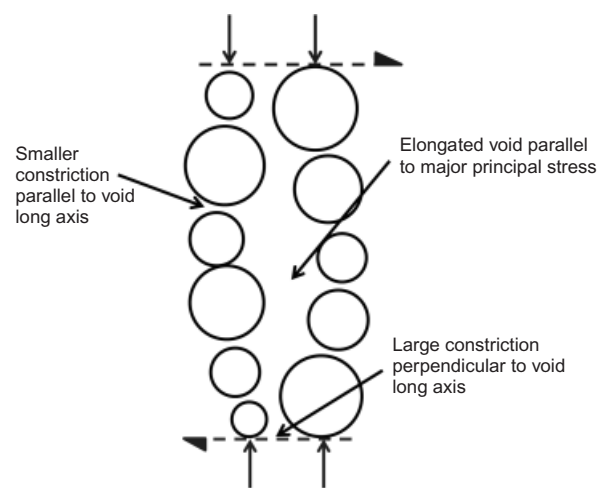


Fig. 8. Conceptual model of void elongation

occur in physical tests is inhibited (e.g. see Thornton (2000)).

Considering the data presented in Figs 5–7 and Table 2, the contact normal orientations are clearly a more sensitive

indicator of stress-induced fabric changes than the void topologies, measured here by considering the constriction sizes. Prior quantitative analysis of void fabric using a scanning line method was discussed by Oda *et al.* (1985) (using experimental data) and Ghedia & O'Sullivan (2012) (using DEM data). Both sets of authors compared the ratio of the maximum and minimum eigenvalues for the contact normals and the voids (termed F_1/F_2 and V_1/V_2 respectively in both cases). Both authors found the maximum change in void fabric (i.e. the maximum change in V_1/V_2) was less than the maximum change in contact normal fabric (i.e. the maximum change in F_1/F_2). While the current data cannot be directly compared with these prior 2D studies that considered the entire void topology, it is important to note the similarity of the trends.

CONCLUSIONS

While a number of studies have quantified fabric anisotropy using particle and contact normal orientations, less consideration has been given to the void phase, probably because of the difficulty associated with defining voids and in particular identifying void boundaries. Here fabric anisotropy was quantified using the inter-void constrictions orientations. The algorithm proposed by Reboul (2008) was used. Data obtained in a series of constant mean stress, true triaxial DEM simulations with stress-induced anisotropy were analysed. The following observations were made.

- (a) The average constriction diameter is larger in the direction of the major principal stress. The larger average constrictions are aligned with a higher concentration of inter-particle contact normals.
- (b) Smaller constrictions ($d_c < d_{c15}$) show a preferential orientation away from the major principal stress direction. It is believed that the preferential orientation of the larger constrictions in the σ_1 and smaller constrictions in the σ_3 directions is because of stress-induced void elongation. Quantifying fabric using the smaller constrictions removes the uncertainty associated with the larger constrictions, which may represent local narrowing of voids, rather than being valid void–void boundaries.
- (c) The constriction size distributions are similar for each shearing mode. However, the intensity of constriction anisotropy, measured by the deviatoric fabric Φ_d , increases in the order TXE > PS > TXC.

REFERENCES

- Al-Raoush, R. T., Willson, K. & Clinton, S. (2003). Comparison of network generation techniques for unconsolidated porous media. *Soil Sci. Soc. Am. J.* **67**, No. 6, 1687.
- Arthur, J. R. F. & Menzies, B. K. (1972). Inherent anisotropy in a sand. *Géotechnique* **22**, No. 1, 115–128, <http://dx.doi.org/10.1680/geot.1972.22.1.115>.
- Barreto, D. (2009). *Numerical and experimental investigation into the behaviour of granular materials under generalised stress states*. PhD thesis, Imperial College London, UK.
- Barreto, D. & O'Sullivan, C. (2012). The influence of inter-particle friction and the intermediate stress ratio on soil response under generalised stress conditions. *Granular Matter* **14**, No. 4, 505–521.
- Barreto, D., O'Sullivan, C. & Zdravkovic, L. (2008). Specimen generation approaches for DEM simulations. *Proc. 4th Int. Symp. Deformation Characteristics Geomater.* **2**, 901–906.
- Barreto, D., O'Sullivan, C. & Zdravkovic, L. (2009). Quantifying the evolution of soil fabric under different stress paths. *Proc. 6th Int. Conf. Micromech. Granular Media, Powder and Grains 2009*, 181–184.
- Behringer, R., Daniels, K. E., Majmudar, T. S. & Sperl, M. (2008). Fluctuations, correlations, and transitions in granular materials: Statistical mechanics for a non-conventional system. *Phil. Trans. R. Soc. A* **366**, No. 1865, 493–504.
- Casagrande, A. & Carillo, N. (1944). Shear failure of anisotropic materials. *J. Boston Soc. Civ. Engrs* **31**, No. 4, 74–87.
- Chan, H. T. & Kenney, T. C. (1973). Laboratory investigation of permeability ratio of New Liskeard varved soil. *Can. Geotech. J.* **10**, No. 3, 453–472.
- Fonseca, J. (2011). *The evolution of morphology and fabric of a sand during shearing*. PhD thesis, Imperial College London, UK.
- Gaudray, G. (2011). *Constriction size distribution and internal erosion*, Scientific Internship Report. Paris, France: Ecole des Ponts ParisTech.
- Ghedia, R. & O'Sullivan, C. (2012). Quantifying void fabric using a scan-line approach. *Comput. Geotech.* **41**, 1–12.
- Haruyama, M. (1981). Anisotropic deformation–strength characteristics of an assembly of spherical particles under three dimensional stresses. *Soils Found.* **21**, No. 4, 41–55.
- Kuwano, R. & Jardine, R. (2002). On the applicability of cross-anisotropic elasticity to granular materials at very small strains. *Géotechnique* **52**, No. 10, 727–749, <http://dx.doi.org/10.1680/geot.2002.52.10.727>.
- Lade, P. V. & Duncan, J. M. (1973). Cubical triaxial tests on cohesionless soil. *J. Soil Mech. Found. Div.* **99**, No. 10, 793–812.
- Ng, T.-T. (2001). Fabric evolution of ellipsoidal arrays with different particle shapes. *J. Engng Mech. ASCE* **127**, No. 10, 994–999.
- Ng, T.-T. (2004a). Shear strength of assemblies of ellipsoidal particles. *Géotechnique* **54**, No. 10, 659–670, <http://dx.doi.org/10.1680/geot.2004.54.10.659>.
- Ng, T.-T. (2004b). Macro- and micro-behaviors of granular materials under different sample preparation methods and stress paths. *Int. J. Solids Struct.* **41**, No. 21, 5871–5884.
- Oda, M., Nemat-Nasser, S. & Konishi, J. (1985). Stress-induced anisotropy in granular masses. *Soils Found.* **25**, No. 3, 85–97.
- Reboul, N. (2008). *Transport de particules dans les milieux granulaires*. PhD thesis, Ecole Centrale de Lyon, France.
- Reboul, N., Vincens, E. & Cambou, B. (2010). A computational procedure to assess the distribution of constriction sizes for an assembly of spheres. *Comput. Geotech.* **37**, No. 1–2, 195–206.
- Rechenmacher, A., Abedi, S. & Chupin, O. (2010). Evolution of force chains in shear bands in sands. *Géotechnique* **60**, No. 5, 343–351, <http://dx.doi.org/10.1680/geot.2010.60.5.343>.
- Rothenburg, L. & Bathurst, R. J. (1989). Analytical study of induced anisotropy in idealized granular materials. *Géotechnique* **39**, No. 4, 601–614, <http://dx.doi.org/10.1680/geot.1989.39.4.601>.
- Roux, J. N. & Combe, G. (2010). How granular materials deform in quasistatic conditions. *AIP Conf. Proc.* **1227**, 260–270.
- Satake, M. (1982). Fabric tensor in granular materials. *Proceedings of the IUTAM conference on deformation and failure of granular materials*, Delft, pp. 63–67.
- Smart, P. (1991). Microstructural classification of clayey sediments. *Geo-Marine Lett.* **11**, No. 3, 170–171.
- Sutherland, H. B. & Mesdary, M. S. (1969). The influence of intermediate principal stress on the strength of sand. *Proc. 7th Int. Conf. Soil Mech. Found. Engng, Mexico* **1**, 391–399.
- Thornton, C. (2000). Numerical simulations of deviatoric shear deformation of granular media. *Géotechnique* **50**, No. 1, 43–53, <http://dx.doi.org/10.1680/geot.2000.50.1.43>.
- Tovey, N. K., Smart, P., Hounslow, M. W. & Leng, X. L. (1992). Automatic orientation mapping of some types of soil fabric. *Geoderma* **53**, No. 3–4, 179–200.